IEICE TRANS. COMMUN., VOL.E87–B, NO.10 OCTOBER 2004

PAPER

Circular Polarization Correlation Coefficient for Detection of Non-natural Targets Aligned Not Parallel to SAR Flight Path in the X-band POLSAR Image Analysis

Koji KIMURA[†], *Student Member*, **Yoshio YAMAGUCHI**[†], **Toshifumi MORIYAMA**[††], *and* **Hiroyoshi YAMADA**[†], *Members*

SUMMARY This paper proposes a method to detect buildings and houses whose walls are not parallel to Synthetic Aperture Radar (SAR) flight path. Experimental observations show that it is difficult to detect these targets because of small backscattering characteristics. The detection method is based on the correlation coefficient in the circular polarization basis, taking full advantage of Polarimetric SAR (POLSAR) data. Since the correlation coefficient is real-valued for natural distributed targets with reflection symmetry and for non-natural targets orthogonal to illumination direction, and it becomes a complex number for non-natural targets aligned not orthogonal to radar Line-Of-Sight (LOS), the value seems to be an effective index for detection of obliquely aligned non-natural targets. The detection results are shown using the X-band Polarimetric and Interferometric SAR (Pi-SAR) single-path data set in conjunction with other polarimetric indices.

key words: *the circular polarization basis, correlation coefficient, phase angle, non-natural targets, Line-Of-Sight, POLSAR*

1. Introduction

High resolution POLSAR data sets have been acquired with fully polarimetric airborne systems such as AIRSAR, Pi-SAR, ESAR, etc. The POLSAR data analysis is carried out to classify land targets as accurate as possible, utilizing the merit of fully polarimetric data.

The purpose of this paper is to show that the correlation coefficient in the right- (r) and left-handed (l) circular polarization basis [1]–[4] is effective for detecting non-natural or man-made targets whose structures are not aligned with SAR flight path. The discrimination between vegetation area, and complex urban block area aligned not orthogonal to radar LOS using POLSAR single-path data is one of the most important and difficult subjects in land cover classification.

Extensive studies [4]–[12] revealed that:

1) $\langle S_{hh}S_{hv}^{*}\rangle$, $\langle S_{vv}S_{hv}^{*}\rangle$ and the corresponding correlation coefficients are almost 0 for natural distributed targets with reflection symmetry. The subscript hv refers to polarization combination with h for horizontal polarization and v for vertical one. The first letter is used for reception and the second letter for transmission based on the definition of scattering matrix. $\langle\bullet\rangle$ and the superscript * denote ensemble average and complex conjugate, respectively. This property applies to microwave frequencies.
2) The L-band frequency penetrates vegetation (grass, bushes, trees, forests, crop fields, etc.). As frequency increases, the penetration becomes small, leading to surface scattering dominant. Thus, the X-band frequency data is highly dominated by surface scattering compared to the L-band data.
3) It is difficult to detect buildings and houses whose walls are aligned not orthogonal to illumination direction (complex urban block area). As shown in Fig. 1, when radar beam hits the wall, most of the reflected wave goes to specular direction. The other scattering process takes place at edge or on irregular surface where co- and cross-polarized components are generated. The polarimetric backscattering characteristics for complex urban block area are similar to those for vegetation area. Radar Cross Section (RCS) is small, and the contribution of double bounce is not so significant. Therefore, the detection of obliquely aligned buildings and houses becomes difficult.

Since the resolution (1.5 m) of the X-band image is finer than that (3 m) of the L-band image for Pi-SAR airborne system, it is worth investigating the X-band capability of detecting land cover targets. In this paper, we pay our attention mainly to the X-band data rather than the L-band one because of high resolution and surface scattering characteristics, properties 1) and 2).

If we use the properties 1) and 2) reversely, it will be

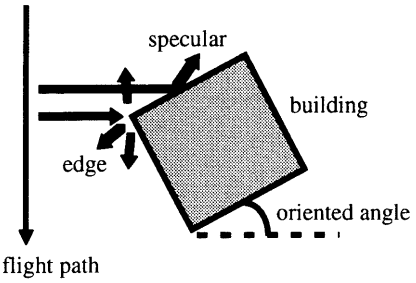

Fig. 1 The scattering from a building whose wall is not parallel to SAR flight path seen from zenith.

Manuscript received November 18, 2003.
Manuscript revised March 1, 2004.

[†]The authors are with Niigata University, Niigata-shi, 950-2181 Japan.
[††]The author is with National Institute of Information and Communications Technology, Koganei-shi, 184-8795 Japan.

possible to pick up non-natural or man-made targets. In this paper, the authors regard non-natural or man-made targets whose structures are not orthogonal to radar LOS as ones with $\langle S_{hh}S^*_{hv}\rangle \neq \langle S_{vv}S^*_{hv}\rangle \neq 0$. The correlation coefficient in the *rl* circular polarization basis becomes a real number for natural distributed targets with reflection symmetry and for non-natural targets (dielectric dihedral corner reflectors) parallel to SAR flight path, while it becomes a complex number for obliquely aligned non-natural targets. Therefore, this index may serve to detect buildings and houses aligned not orthogonal to illumination direction.

This index can be obtained by elements of ensemble averaged covariance matrix in the *rl* basis. The ensemble average processing is carried out on 9 by 9 pixel window for obtaining this index. As preprocessing for target detection, polarimetric calibration [5] is applied to POLSAR data. The POLSAR data utilized here is the X-band Pi-SAR single-path data of the western part in Niigata City.

Section 2 describes a brief principle of obtaining correlation coefficient in the *rl* basis. Section 3 shows the X-band Pi-SAR single-path data for analysis, and target detection results.

2. Correlation Coefficient in the RL Basis

Polarimetric radar measures scattering matrix with quad-polarizations. The scattering matrix in the *hv* linear polarization basis can be expressed as

$$[S(hv)] = \begin{bmatrix} S_{hh} & S_{hv} \\ S_{vh} & S_{vv} \end{bmatrix}. \tag{1}$$

For the reciprocal backscattering case, $S_{hv} = S_{vh}$.

The scattering vector $\boldsymbol{S}_{i(hv)}$ based on the scattering matrix elements for the ith pixel is defined by the following equation [4]–[9].

$$\boldsymbol{S}_{i(hv)} = \begin{bmatrix} S_{hh} \\ \sqrt{2}S_{hv} \\ S_{vv} \end{bmatrix}. \tag{2}$$

A one-look covariance matrix, $C_{i(hv)}$, for the ith pixel, is formed by the scattering vector $\boldsymbol{S}_{i(hv)}$.

$$C_{i(hv)} = \boldsymbol{S}_{i(hv)}\boldsymbol{S}^{\dagger}_{i(hv)}, \tag{3}$$

where the superscript † denotes complex conjugate transpose. The ensemble averaged covariance matrix, $\langle C\rangle_{hv}$, is obtained by averaging n neighboring pixels [4]–[9].

$$\langle C\rangle_{hv} = \frac{1}{n}\sum_{i=1}^{n} C_{i(hv)}. \tag{4}$$

The scattering matrix elements in the right- (r) and left-handed (l) circular polarization basis [1]–[4] can be derived by the following transformation:

$$\begin{aligned}[S(rl)] &= \begin{bmatrix} S_{rr} & S_{rl} \\ S_{lr} & S_{ll} \end{bmatrix} \\ &= \frac{1}{2}\begin{bmatrix} 1 & -j \\ -j & 1 \end{bmatrix}[S(hv)]\begin{bmatrix} 1 & -j \\ -j & 1 \end{bmatrix}. \end{aligned} \tag{5}$$

Therefore, the ensemble averaged covariance matrix $\langle C\rangle_{rl}$ is obtained as follows:

$$\langle C\rangle_{rl} = \frac{1}{n}\sum_{i=1}^{n} \boldsymbol{S}_{i(rl)}\boldsymbol{S}^{\dagger}_{i(rl)}, \tag{6}$$

where

$$\boldsymbol{S}_{i(rl)} = \frac{1}{2}\begin{bmatrix} 1 & -j\sqrt{2} & -1 \\ -j\sqrt{2} & 0 & -j\sqrt{2} \\ -1 & -j\sqrt{2} & 1 \end{bmatrix}\begin{bmatrix} S_{hh} \\ \sqrt{2}S_{hv} \\ S_{vv} \end{bmatrix}. \tag{7}$$

The correlation coefficient in arbitrary *ab* polarization basis is represented as

$$\begin{aligned}\gamma_{aabb} &= \frac{\langle S_{aa}S^*_{bb}\rangle}{\sqrt{\langle S_{aa}S^*_{aa}\rangle}\sqrt{\langle S_{bb}S^*_{bb}\rangle}} \\ &= |\gamma_{aabb}|\exp(j\phi_{aabb}). \end{aligned} \tag{8a}$$

The index in the *hv* linear and *rl* circular polarization basis can be expressed as

$$\begin{aligned}\gamma_{hhhv} &= \frac{\langle S_{hh}S^*_{hv}\rangle}{\sqrt{\langle S_{hh}S^*_{hh}\rangle}\sqrt{\langle S_{hv}S^*_{hv}\rangle}} \\ &= |\gamma_{hhhv}|\exp(j\phi_{hhhv}), \end{aligned} \tag{8b}$$

$$\begin{aligned}\gamma_{rrll} &= \frac{\langle S_{rr}S^*_{ll}\rangle}{\sqrt{\langle S_{rr}S^*_{rr}\rangle}\sqrt{\langle S_{ll}S^*_{ll}\rangle}} \\ &= |\gamma_{rrll}|\exp(j\phi_{rrll}). \end{aligned} \tag{8c}$$

The phase angle ϕ_{rrll} in Eq. (8c) is represented in terms of the *hv* components as

$$\phi_{rrll} = \tan^{-1}\frac{\left\langle \mathrm{Re}\left\{4S^*_{hv}(S_{hh}-S_{vv})\right\}\right\rangle}{\langle 4|S_{hv}|^2 - |S_{hh}-S_{vv}|^2\rangle}. \tag{8d}$$

It is known for natural distributed targets with reflection symmetry [4]–[8], [10], [11] that $\langle S_{hh}S^*_{hv}\rangle \approx \langle S_{vv}S^*_{hv}\rangle \approx 0$ (hence $|\gamma_{hhhv}| \approx 0$), and the phase angle ϕ_{hhhv} is uniformly distributed in $[-\pi, \pi]$. This property applies to microwave frequency bands. Under the condition $\langle S_{hh}S^*_{hv}\rangle \approx \langle S_{vv}S^*_{hv}\rangle \approx 0$, the correlation coefficient in Eq. (8c) can be approximated as

$$\gamma_{rrll} = \frac{\left\langle 4|S_{hv}|^2\right\rangle - \left\langle |S_{hh}-S_{vv}|^2\right\rangle}{\langle 4|S_{hv}|^2\rangle + \langle |S_{hh}-S_{vv}|^2\rangle}. \tag{9}$$

It should be noted that γ_{rrll} is real-valued, and that ϕ_{rrll} is 0 or π depending on the magnitude balance between $\langle 4|S_{hv}|^2\rangle$ and $\langle |S_{hh}-S_{vv}|^2\rangle$. If $\langle 4|S_{hv}|^2\rangle \ll \langle |S_{hh}-S_{vv}|^2\rangle$ or $\langle 4|S_{hv}|^2\rangle \gg \langle |S_{hh}-S_{vv}|^2\rangle$, the corresponding target area exhibits high correlation. In contrast, the correlation becomes low if $\langle 4|S_{hv}|^2\rangle \approx \langle |S_{hh}-S_{vv}|^2\rangle$. When γ_{rrll} becomes a complex number after the calculation of Eq. (8c), the corresponding area contains non-natural targets (buildings and houses) whose structures are not aligned with SAR flight path. As shown in Eq. (8d), the expression for ϕ_{rrll} includes the effect of reflection symmetry. γ_{rrll} becomes a complex number when $\mathrm{Re}\{4S^*_{hv}(S_{hh}-S_{vv})\} \neq 0$ in Eq. (8d). The

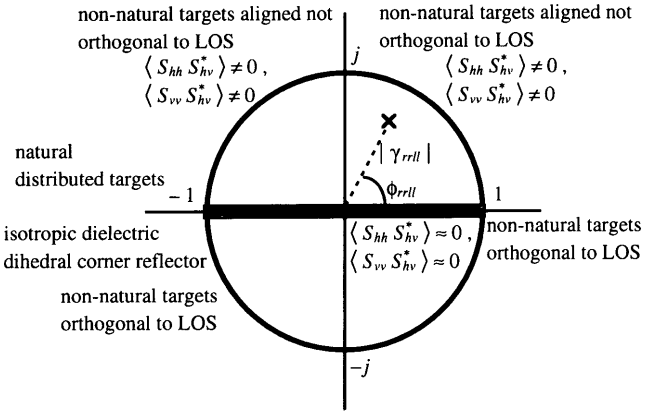

Fig. 2 The behavior of γ_{rrll}.

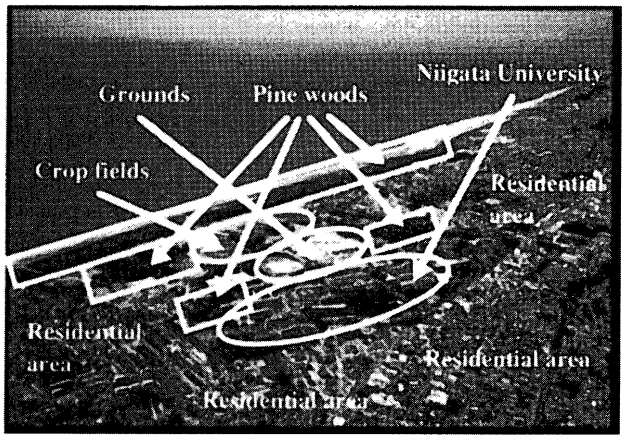

Fig. 3 Photo around Niigata University.

restriction imposed on $\mathrm{Re}\{4S_{hv}^*(S_{hh} - S_{vv})\} \neq 0$ indicates highly complex scattering nature since there exist no canonical basic targets (sphere, dihedral, etc.).

The behavior of γ_{rrll} is illustrated in Fig. 2. For targets with $\langle S_{hh}S_{hv}^* \rangle \approx \langle S_{vv}S_{hv}^* \rangle \approx 0$, γ_{rrll} is plotted on real axis in the complex plane. For targets with $\langle S_{hh}S_{hv}^* \rangle \neq \langle S_{vv}S_{hv}^* \rangle \neq 0$, the index is located within the unit circle, except on the real axis. It can be seen in this figure that $|\gamma_{rrll}|$ and ϕ_{rrll} have more information than $|\gamma_{hhhv}|$ and ϕ_{hhhv}.

It is expected that γ_{rrll} is an effective index for detecting complex urban block area which is not orthogonal to illumination direction. The discrimination between vegetation and complex urban block area is one of the most important and difficult subjects in land cover classification, since the polarimetric backscattering characteristics are similar (small RCS, cross-polarized component return to radar, and little contribution of double bounce) and the classification errors occur in these two areas.

3. Polarimetric Scattering Characteristics for the Analyzed Site

The authors analyzed the X-band Pi-SAR image data set (Data No. 6012) provided by CRL/NASDA, which is an image of the western part in Niigata City, Japan. The scene around university campus contains residential area, the Sea of Japan, river, crop fields, pine woods, etc. The residential area and university buildings are aligned not parallel to SAR flight path. Figure 3 shows photo around the university campus. As preprocessing for land target detection, polarimetric calibration [5] is carried out on the Pi-SAR data.

The X-band composite image based on the polarimetric target vector [6]–[9], [12] is shown in Fig. 4. The $|S_{hh} - S_{vv}|$ (red), $2|S_{hv}|$ (green), and $|S_{hh} + S_{vv}|$ (blue) component correspond to double bounce, cross-polarized component and single bounce, respectively. The figure illustrates the cross-polarized component highly contributes to backscattering from land targets around the university campus, i.e., volume and edge scattering occur significantly. The backscattering characteristics for residential area are similar to those for vegetated area. For the analysis, the authors picked up

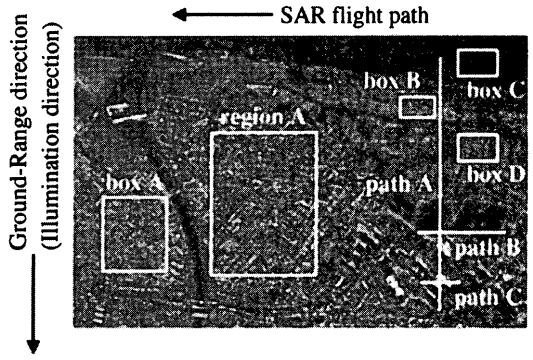

Fig. 5 Analyzed region, targets and paths.

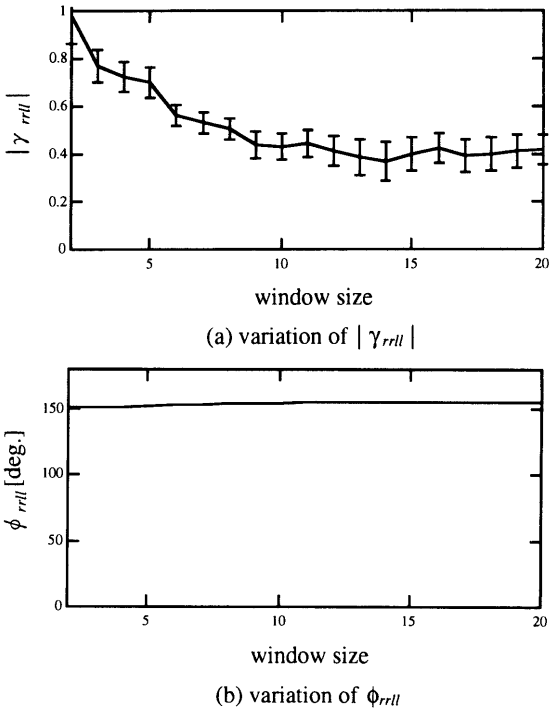

Fig. 6 The variation of $|\gamma_{rrll}|$ and ϕ_{rrll} as a function of window size.

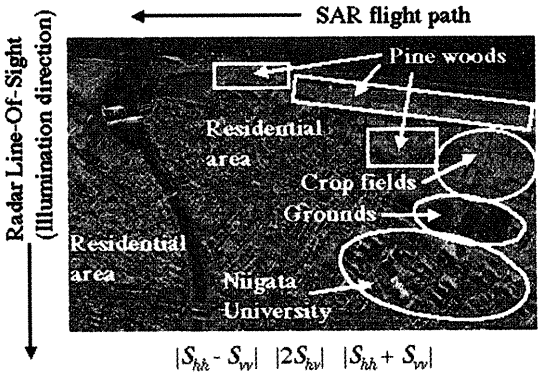

Fig. 4 The X-band composite image based on polarimetric target vector.

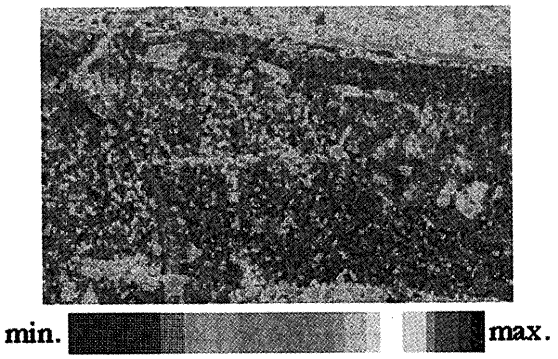

(a) H

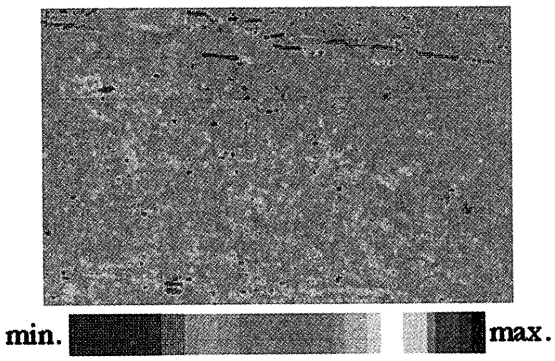

(b) $\bar{\alpha}$

Fig. 8 The X-band polarimetric entropy and alphabar image.

Fig. 10 The overlay image of ϕ_{rrll} and polarimetric target vector $\left(-\frac{3}{4}\pi \leq \phi_{rrll} \leq \frac{3}{4}\pi\right)$.

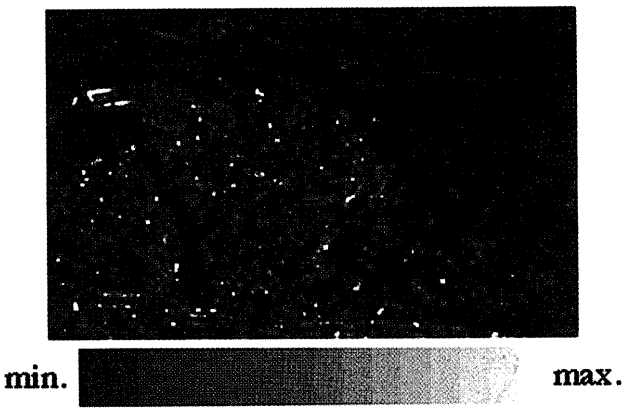

(a) $|\gamma_{hhhv}|$

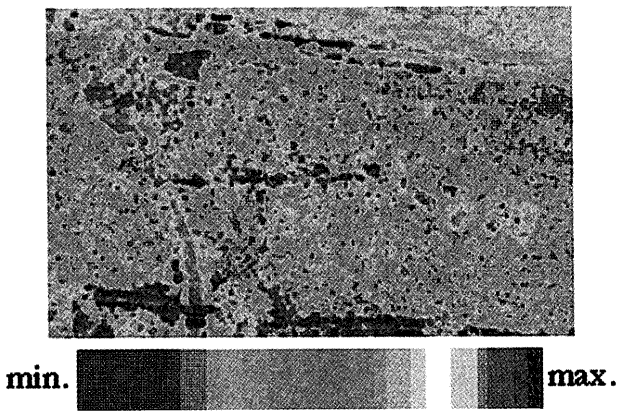

(b) $|\gamma_{rrll}|$

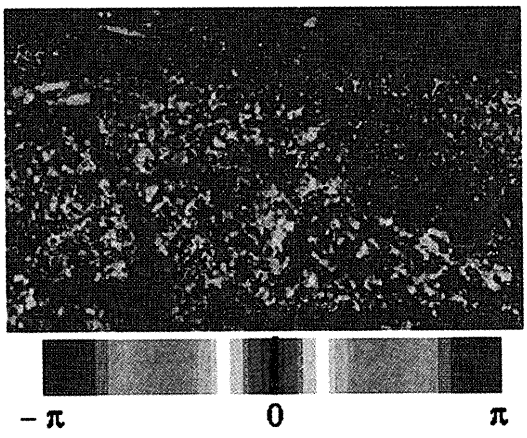

(c) ϕ_{rrll}

Fig. 7 The X-band images of $|\gamma_{hhhv}|$, $|\gamma_{rrll}|$ and ϕ_{rrll}.

several regions, targets and paths shown in Fig. 5.

The ensemble average processing needs to obtain γ_{rrll}. Figures 6(a) and (b) illustrate the variation of $|\gamma_{rrll}|$ (average and standard deviation) and ϕ_{rrll} (average) as a function of window size for region A (part of complex residential area) shown in Fig. 5, respectively. It is seen in Fig. 6(a) that the average of $|\gamma_{rrll}|$ becomes approximately constant over 9 by 9 window size. Figure 6(b) shows that the average of ϕ_{rrll} is insensitive to window size. Therefore, the authors carried out the ensemble average processing on 9 by 9 window size in POLSAR data.

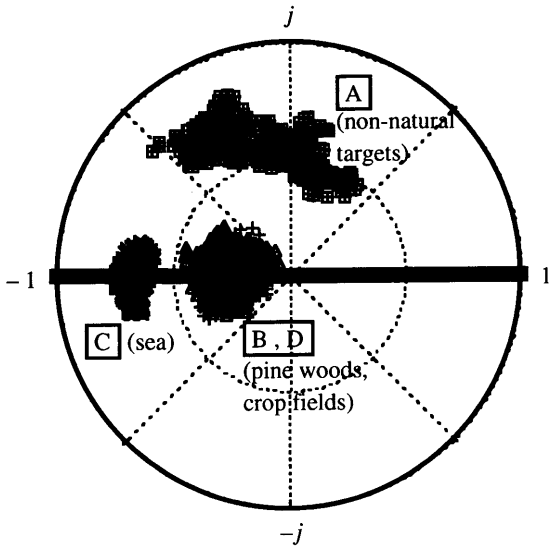

Fig. 9 Distribution of γ_{rrll} for boxes A–D.

Figure 7(a) illustrates the X-band $|\gamma_{hhhv}|$ image. It is seen in this figure that $|\gamma_{hhhv}|$ becomes nearly 0 for natural distributed targets including the Sea of Japan, river, crop fields and pine woods. The index is not 0 for part of residential area and non-natural targets such as bridges, floodgate, etc. However, it is seen in this figure that non-natural targets are not fully detected. Especially, the university buildings do not appear in this figure.

Figure 7(b) shows $|\gamma_{rrll}|$ image. It is seen in Fig. 7(b) that the natural distributed targets with $\langle S_{hh}S_{hv}^{*}\rangle \approx \langle S_{vv}S_{hv}^{*}\rangle \approx 0$ except pine woods and crop fields, and dielectric dihedral corner reflectors orthogonal to radar LOS (part of residential area, bridges and floodgate) exhibit high correlation since $\langle 4|S_{hv}|^2\rangle \ll \langle |S_{hh} - S_{vv}|^2\rangle$. Especially, the correlation is high for non-natural targets orthogonal to illumination direction, which means that $|\gamma_{rrll}|$ detects these targets. The index is low for vegetated area and for non-natural target area aligned not parallel to SAR flight path, since the contribution of cross-polarized component as well as that of co-polarized one is significant.

Figure 7(c) illustrates ϕ_{rrll} image. The regions are colored by the phase angle with blue ($\phi_{rrll} = \pm\pi$), green ($\phi_{rrll} = \pm\frac{\pi}{2}$) and red ($\phi_{rrll} = 0$) respectively in this figure. It is seen in Fig. 7(c) that non-natural targets aligned not orthogonal to illumination direction are detected. The complex residential area and university campus containing buildings and houses whose walls are not parallel to SAR flight path are detected. The phase angle ϕ_{rrll} becomes nearly π for the natural targets with $\langle S_{hh}S_{hv}^{*}\rangle \approx \langle S_{vv}S_{hv}^{*}\rangle \approx 0$, and dielectric dihedral corner reflectors orthogonal to radar LOS (part of residential area, bridges and floodgate). In contrast, the index becomes different from π for the residential area and university buildings, which are aligned not orthogonal to radar LOS.

Figure 8 shows the polarimetric entropy (H) and alphabar ($\bar{\alpha}$) images [6]–[9], [12]. This figure shows that

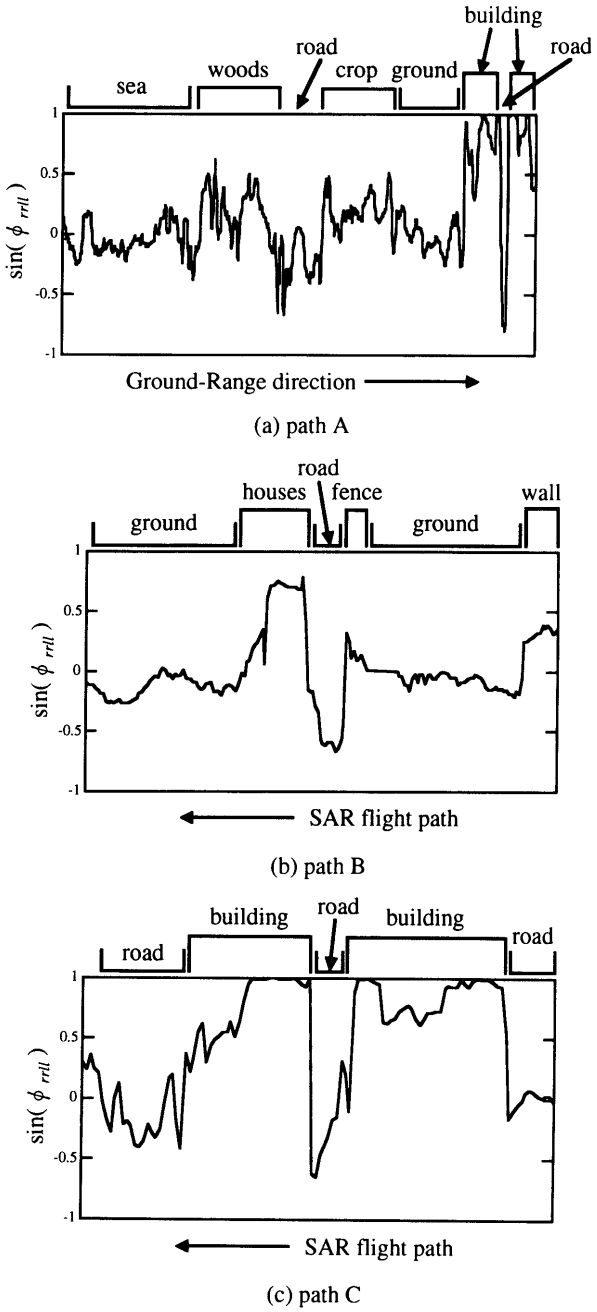

Fig. 11 Contour plots of $\sin(\phi_{rrll})$ for three paths A–C.

the university buildings, residential area and vegetated area around the university campus exhibit similar polarimetric backscattering characteristics with high H and moderate $\bar{\alpha}$. Therefore, it is difficult to discriminate vegetated targets and non-natural targets aligned not orthogonal to illumination direction using H and $\bar{\alpha}$ only.

Figure 9 illustrates the distribution of γ_{rrll} in the complex plane. The authors picked up four boxes A–D shown in Fig. 5:

box A: non-natural targets whose structures are not parallel to SAR flight path,
box B: pine woods,

box C: the Sea of Japan,
box D: crop fields.

It is seen that γ_{rrll} is plotted near negative real axis for natural distributed targets B–D, while the index deviates from the negative real axis for non-natural target A in the complex plane. The correlation is high in box C, while natural distributed targets B and D exhibit low correlation. $|\gamma_{rrll}|$ is from 0.3 to 0.75 in box A. γ_{rrll} represents the scattering characteristics for each target well.

Figure 10 illustrates the overlay image of binary ϕ_{rrll} image and the composite image shown in Fig. 4. The threshold value is set $-\frac{3}{4}\pi \leq \phi_{rrll} \leq \frac{3}{4}\pi$ based on the property of ϕ_{rrll} and on Fig. 9 to exclude natural target contribution. It is seen in Fig. 10 that the method based on the phase angle ϕ_{rrll} performs well on detecting buildings and houses aligned not orthogonal to radar LOS. Especially, the university buildings are well detected.

The contour plots of $\sin(\phi_{rrll})$ for natural and non-natural targets are illustrated in Fig. 11. The authors picked up three paths A–C as shown in Fig. 5:

path A: the Sea of Japan - pine woods - road - crop fields - ground - building - road - building,
path B: ground - houses - road - fence - ground - concrete wall,
path C: road - building - road - building - road.

It is seen in this figure that $\sin(\phi_{rrll})$ becomes large for non-natural targets such as building, house, concrete wall, etc. These three plots show that ϕ_{rrll} is useful for detection of non-natural targets aligned not parallel to SAR flight path.

The analysis results show that γ_{rrll} derived from the X-band POLSAR single-path data is a useful index for detecting non-natural targets whose structures are not orthogonal to illumination direction. The index is suited for detecting complex residential area, where the polarimetric backscattering characteristics are similar to those for vegetated area.

4. Conclusion

The method of detecting buildings and houses whose walls are not parallel to SAR flight path based on the correlation coefficient in the *rl* basis in the X-band Pi-SAR single-path data was proposed in this paper. The index is derived by ensemble averaged covariance matrix in the *rl* basis. The comparison with the detection results based on other representative indices using the X-band Pi-SAR single-path data shows that γ_{rrll} is useful for the detection.

Acknowledgments

The authors would like to thank NASDA and CRL for providing valuable Pi-SAR image data sets. This work in part was supported by Grant in Aid for Scientific Research, JSPS, Japan.

References

[1] E. Hanle, "New contemplations on polarimetric decomposition based on expected target orientation," Proc. 4th International Workshop on Radar Polarimetry, pp.67–76, July 1998.
[2] M. Murase, Y. Yamaguchi, and H. Yamada, "Polarimetric correlation coefficient applied to tree classification," IEICE Trans. Electron., vol.E84-C, no.12, pp.1835–1840, Dec. 2001.
[3] Y. Yamaguchi, K. Kimura, and H. Yamada, "ALOS-PALSAR image simulation in various polarization basis," International Geoscience and Remote Sensing Symposium 2002, CD-ROM, June 2002.
[4] C.T. Schnaider, "Polarimetric analysis of RAMSES SAR images," Proc. 4th International Workshop on Radar Polarimetry, pp.366–375, July 1998.
[5] S. Quegan, "A unified algorithm for phase and cross-talk calibration of polarimetric data-theory and observation," IEEE Trans. Geosci. Remote Sens., vol.32, no.1, pp.89–99, Jan. 1994.
[6] Y. Jin and F. Chen, "Polarimetric scattering indexes and information entropy of the SAR imagery for surface monitoring," IEEE Trans. Geosci. Remote Sens., vol.40, no.11, pp.2502–2506, Nov. 2002.
[7] S.R. Cloude and E. Pottier, "A review of target decomposition theorems in radar polarimetry," IEEE Trans. Geosci. Remote Sens., vol.34, no.2, pp.498–518, March 1996.
[8] S.R. Cloude, I. Hajnsek, and K.P. Papathanassiou, "An eigenvector method for the extraction of surface parameters in polarimetric SAR," Proc. CEOS SAR Workshop, ESA SP-450, pp.693–698, Toulouse, France, March 2000.
[9] L. Ferro-Famil, E. Pottier, and J.S. Lee, "Unsupervised classification of multifrequency and fully polarimetric SAR images based on the H/A/Alpha-Wishart classifier," IEEE Trans. Geosci. Remote Sens., vol.39, no.11, pp.2332–2342, Nov. 2001.
[10] J.J. van Zyl, "Unsupervised classification of scattering mechanisms using radar polarimetry data," IEEE Trans. Geosci. Remote Sens., vol.27, no.1, pp.36–45, Jan. 1989.
[11] A. Freeman and S. Durden, "A three-component scattering model for polarimetric SAR data," IEEE Trans. Geosci. Remote Sens., vol.36, no.3, pp.963–973, May 1998.
[12] S.R. Cloude and E. Pottier, "An entropy based classification scheme for land applications of polarimetric SAR," IEEE Trans. Geosci. Remote Sens., vol.35, no.1, pp.68–78, Jan. 1997.

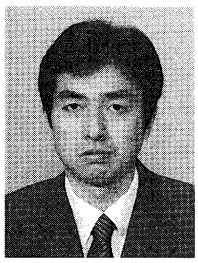

Koji Kimura was born in Niigata, Japan, on March 1, 1976. He received the B.E. and M.E. degrees from Niigata University, Niigata, Japan, in 1998 and 2000, respectively. He is currently working toward the Ph.D. degree in information engineering at the same University. He is now engaged in SAR image analysis and target classification using radar polarimetry.

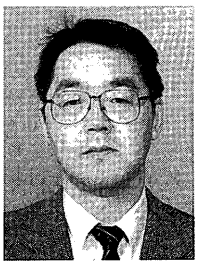

Yoshio Yamaguchi received the B.E. degree in electronics engineering from Niigata University in 1976, and the M.E. and Dr.Eng. degrees from Tokyo Institute Technology in 1978 and 1983, respectively. In 1988, he joined the Faculty of Engineering, Niigata University, where he is a professor. From 1988 to 1989, he was a Research Associate at the University of Illinois, Chicago. His interests are in the field of propagation characteristics of electromagnetic waves in lossy medium, radar polarimetry, microwave remote sensing and imaging. Dr. Yamaguchi is a fellow of IEEE, and a member of the Japan Society for Snow Engineering.

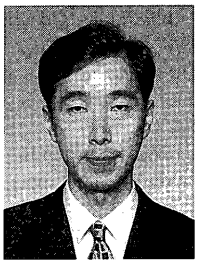

Toshifumi Moriyama was born in Fukui Prefecture, Japan, on January 1, 1972. He received the B.E., M.E. and Ph.D. degrees in Information Engineering from Niigata University, Japan, in 1994, 1995 and 1998, respectively. He was with Fujitsu System Integration Laboratories Ltd. from 1998 to 2003. He is now with National Institute of Information and Communications Technology. His current research involves radar polarimetry and microwave remote sensing. He is a member of IEEE and Remote Sensing Society of Japan.

Hiroyoshi Yamada received the B.E., M.E. and Dr.Eng. degrees from Hokkaido University, Sapporo, Japan, in 1988, 1990 and 1993, respectively, all in electronic engineering. In 1993, he joined the Faculty of Engineering, Niigata University, where he is an associate professor. From 2000 to 2001, he was a Visiting Scientist at Jet Propulsion Laboratory, California Institute of Technology, Pasadena. His current interests involve in the field of array signal processing, radar polarimetry and interferometry, microwave remote sensing and imaging. Dr. Yamada is a member of IEEE.